Meander Centerline Migration Model (MCMM)

Padova, September 12, 2017

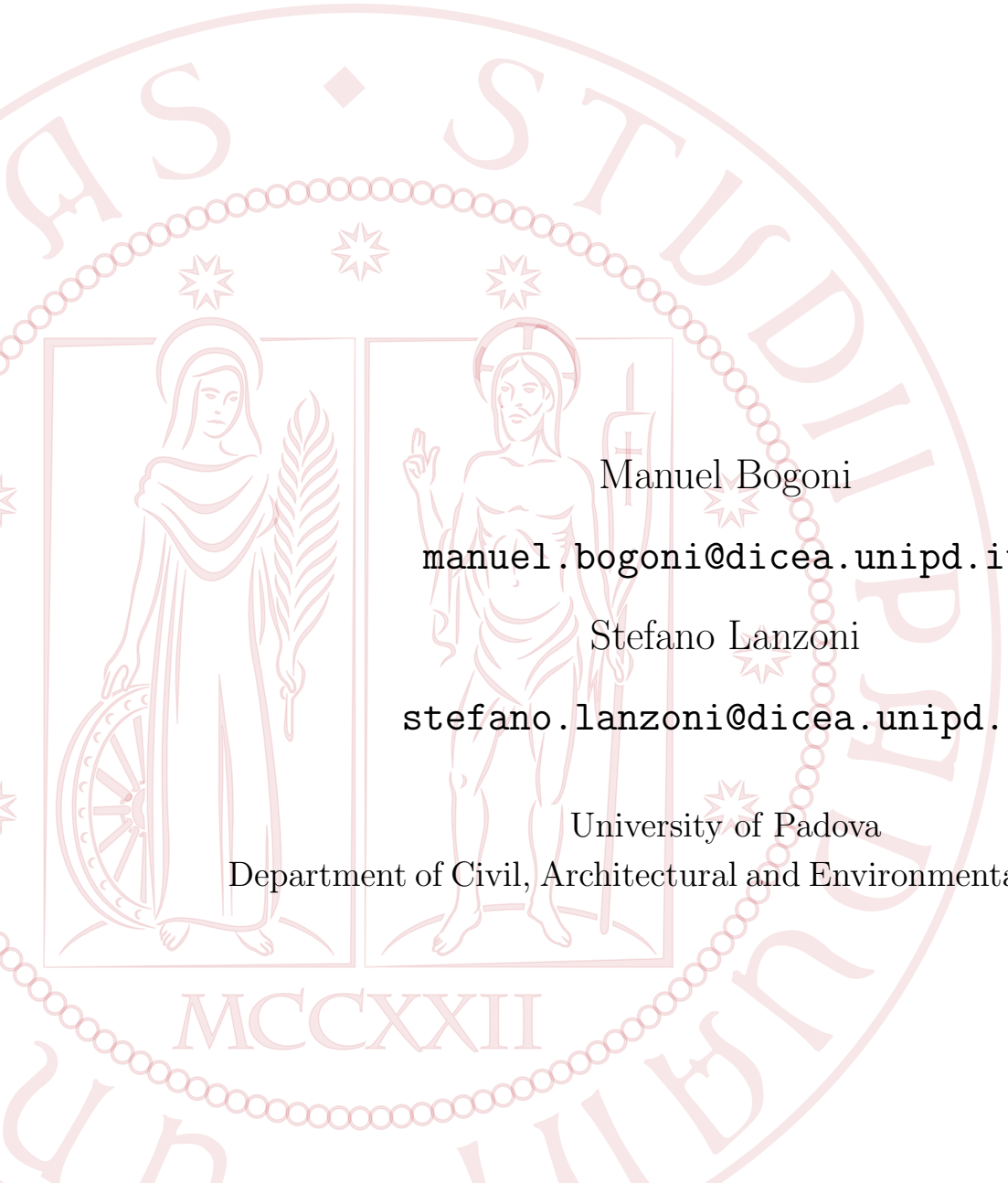

Manuel Bogoni

manuel.bogoni@dicea.unipd.it

Stefano Lanzoni

stefano.lanzoni@dicea.unipd.it

University of Padova
Department of Civil, Architectural and Environmental Engineering

Contents

1 Intro

The MCMM, namely the Meander Centerline Migration Model, simulates the long-term evolution of a meandering river flowing above a heterogeneous self-formed floodplain. On one hand, the structure of the floodplain surface builds up and modifies because of the river migration leading to neck cutoff process and forming oxbow lakes and scroll bars. On the other hand, the river migration is affected by the heterogeneous distribution of the floodplain erodibility given by the presence of the above-mentioned environments on the floodplain surface.

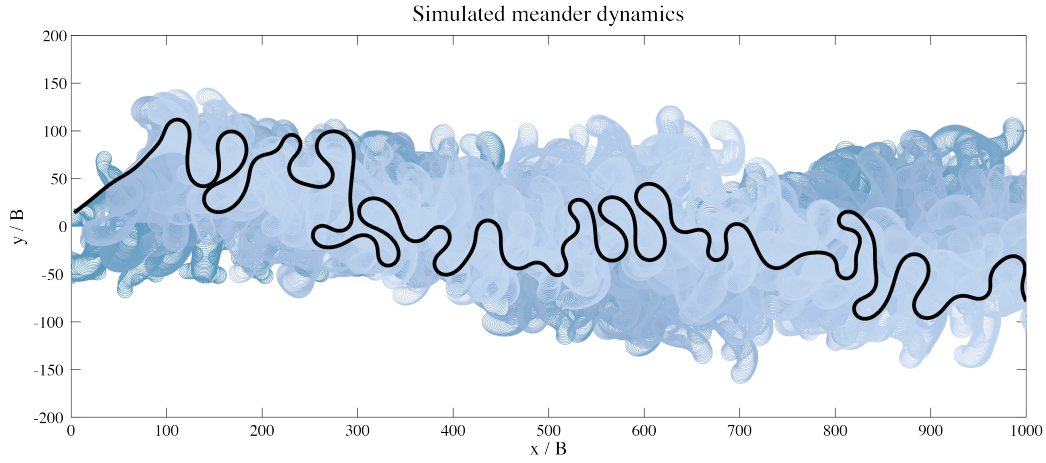

2 Mathematical modelling of meander dynamics

This section is based on the work of Bogoni (2017) and outlines the mathematical and numerical tools required to build a model able to handle the long-term migration of meandering rivers flowing above heterogeneous floodplains. The main quantities and variables involved in the problem are outlined in Section 2. The frame of the numerical modelling builds upon other models available in literature, e.g. Camporeale et al. (2005); Lanzoni et al. (2006); Lanzoni and Seminara (2006); Frascati and Lanzoni (2009). It consists of a migration model for the river axis, a model for the floodplain structure, and a morphodynamic model for the curvature-driven flow field.

References and notations

With reference to the sketch of Figure 1, let (x^*, y^*, z^*) be a Cartesian reference system where x^* is the longitudinal flow direction, and (s^*, n^*, z^*) be a orthogonal intrinsic reference system. Hereafter the superscript * will denote dimensional quantities. Moreover, R^* is the local curvature radius of the river axis, and θ the local angle of the axis tangent with respect to the longitudinal direction. The curvature by definition is $\mathcal{C}^* = 1/R^*$. As far as the channel cross section is concerned, $2B_0^*$ and D_0^* are the width and the depth of a reference straight rectangular channel having the same flow discharge, $2B_0^* D_0^* U_0^*$, bed slope S, and characteristic grain size d_s^* of the considered meandering river (e.g., d_{50}^*), with U_0^* the cross-sectionally averaged velocity. In addition, η^* and H^* are the local bed elevation and the free surface elevation with respect to a given datum, while $D^* = H^* - \eta^*$ is the local flow depth. The local velocity components along the longitudinal, transverse and vertical direction are u^*, v^*, and w^*, respectively.

The next step is to scale the above relevant quantities through the uniform flow parameters. Hence:

$$(x^*, y^*, s^*, n^*, R^*) = B_0^* (x, y, s, n, R) \tag{1a}$$

$$(z^*, \eta^*, H^*, D^*) = D_0^* (z, \eta, H, D) \tag{1b}$$

$$(u^*, v^*, w^*) = U_0^* (u, v, w) \tag{1c}$$

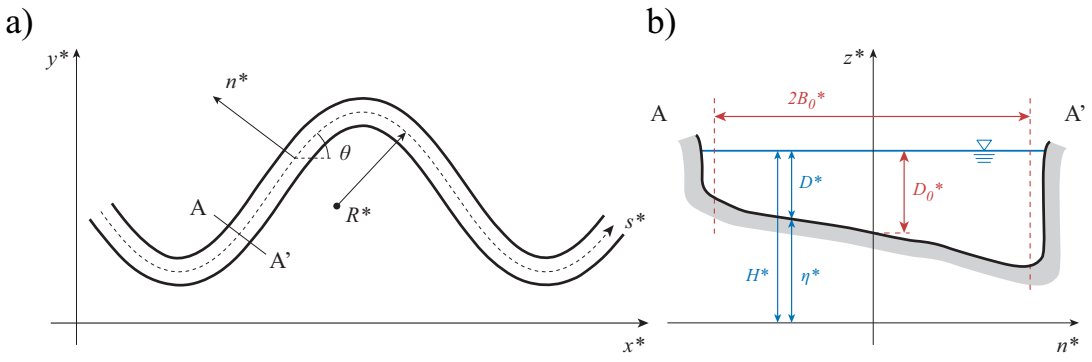

Figure 1: Reference systems and notation for a) the river planform and b) the cross-section.

A curvature parameter may be defined as follows:

$$\nu_0 = \frac{B_0^*}{R_0^*} \tag{2}$$

where R_0^* is a reference radius of channel axis curvature, e.g. the minimum value attained along the investigated reach. The fundamental hypothesis for deriving the mathematical model is that ν_0 is a small parameter, i.e. the river planforms are made by sufficiently gentle and wide bends such that the local curvature radius is much larger than the cross section width. The dimensionless local curvature $\mathcal{C}$ turns out to be (Frascati and Lanzoni, 2013):

$$\mathcal{C} = -\frac{1}{\nu_0}\frac{\partial \theta}{\partial s} \tag{3}$$

The relevant morphological parameters are the half width to depth ratio β, the Shields number τ_* and the dimensionless grain size d_s, defined as follows:

$$\beta = \frac{B_0^*}{D_0^*} \tag{4a}$$

$$\tau_* = \frac{C_f U_0^{*2}}{\Delta g d_s^*} \tag{4b}$$

$$d_s = \frac{d_s^*}{D_0^*} \tag{4c}$$

where g is the gravity acceleration, $\Delta = (\rho_s - \rho)/\rho$ is the submerged specific gravity of the sediment ($\rho_s \simeq 2650$ kg / m^3, $\rho = 1000$ kg / m^3), and C_f is the friction coefficient.

Velocity and depth are related together through the Froude number:

$$F_0 = \frac{U_0^*}{\sqrt{gD_0^*}} \tag{5}$$

Finally, the sediment motion leads to a volumetric discharge per unit width denoted as q_s^*, which may be scaled as:

$$\Phi = \frac{q_s}{R_p \nu} \tag{6}$$

where $\nu \simeq 10^{-6}$ m^2/s is the kinematic viscosity of water, and R_p is the Reynolds particle number:

$$R_p = \frac{\sqrt{g\Delta} d_s^{*3/2}}{\nu} \tag{7}$$

Hereafter, under dominant bedload transport Φ is computed through the formula of Parker (1990). The particle Reynolds number, which controls the intensity of suspended load transport (see, e.g., Frascati and Lanzoni, 2010) is also considered to evaluate the threshold above which suspended load takes place (Van Rijn, 1984a). In this case the total load predictor of Engelund and Hansen (1967) is used to compute Φ. Moreover, R_p is used to establish whether the river bed is flat or dune-covered (Van Rijn, 1984b) when computing the friction coefficient C_f through the method of Engelund and Hansen (1967).

The long-term migration of the river

The long-term migration of river planforms is driven by the complex interplay of the processes of erosion at the inner bank and deposition at the outer bank, possibly leading to spatial and temporal variation of the local channel width. Among others, the affecting factors may be the type of bank failure, the composition of the banks and of the slumped block material, and the vegetation properties. The erosion and deposition processes usually occur at different times and different time scales (Asahi et al., 2013). However, many meandering rivers tend to have a near constant width as channel sinuosity evolves (Parker et al., 2011), showing a normal distribution of channel widths when the fluvial system is subjected to a steady-forcing discharge (Wickert et al., 2013). Eventually, the typical ridge-and-swale bar topography develops (van De Lageweg et al., 2014). This scenario requires an active communication between bank

erosion at the outer bend, i.e. bank pull, and bank growth at the inner bend, i.e. bank push (Eke et al., 2014; van De Lageweg et al., 2014; Schuurman et al., 2016). As a consequence, a constant width of the river cross section may be assumed as a first approximation, and the river path may be described by its centerline.

Referring to the planimetric sketch of Figure 1, the configuration of the channel axis at a certain time t may be described by the current distribution of angles $\theta\left(s^*, n^*\right)$ formed by the local tangent to the channel axis with the longitudinal direction. Indeed, Seminara et al. (2001) demonstrated that the planimetric evolution at the generic location s along the river axis is described by the following integro-differential equation:

$$\frac{\partial \zeta}{\partial s} = \frac{\partial \theta}{\partial t} - \frac{\partial \theta}{\partial s} \int_0^s \zeta \frac{\partial \theta}{\partial s} ds \tag{8}$$

where the lateral migration velocity ζ and the time t are scaled as:

$$\zeta^* = U_0^* \zeta \tag{9a}$$

$$t^* = \frac{U_0^*}{B_0^*} t \tag{9b}$$

Equation (8) drives the lateral migration of the river path across the floodplain over the time, producing a local displacement $\xi_n\left(s\right)$ normal to the channel axis:

$$\frac{d\xi_n\left(s\right)}{dt} = \zeta\left(s\right) \tag{10}$$

Because of the previous assumption of nearly constant cross section width, the relation proposed by Ikeda et al. (1981) to model the river migration across the valley surface may be assumed. In dimensionless form, the relation reads:

$$\zeta = E\, U_b \tag{11}$$

where E is a dimensionless long-term erosion coefficient, while $U_b = U_b^*/U_0^*$ is the dimensionless excess near-bank velocity, i.e. the difference between the longitudinal velocity $U\big|_{n=1}$ at the outer bank ($n = n^*/B_0^* = 1$) and the longitudinal velocity $U\big|_{n=-1}$ at the inner bank ($n = n^*/B_0^* = -1$) All the involved terms are function of the coordinate s along the river centerline.

The problem outlined so far is solved numerically by discretizing the dimensionless river centerline s through a polyline made by N points $P_i(x_i, y_i)$, defined with respect

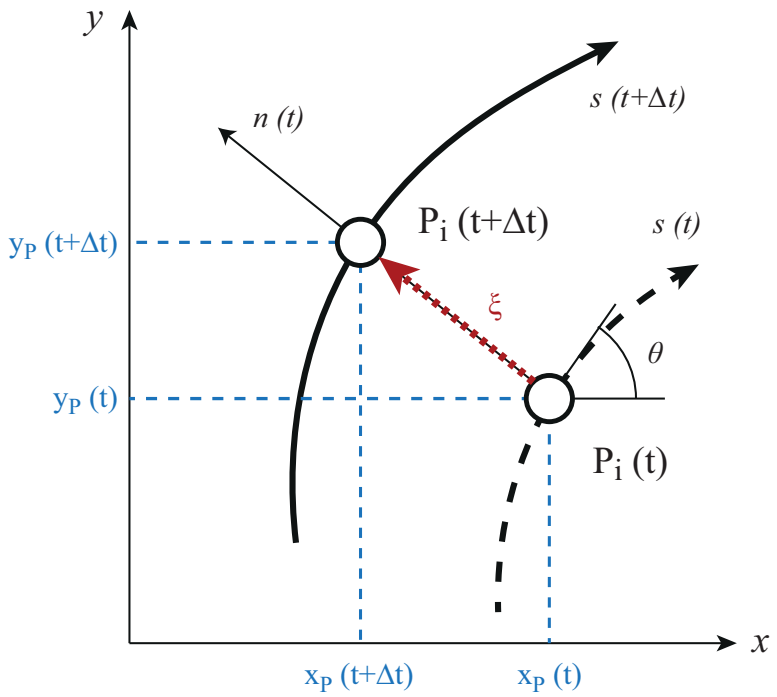

Figure 2: Sketch of the migration of a point P lying on the channel axis, due to the displacement from the configuration $s(t)$ to the new configuration $s(t + \Delta t)$. Quantities may be either dimensional or dimensionless, the scaling factor being B_0^*.

to the Cartesian reference system of Figure 1. As described by the sketch in Figure 2, the differential equation (10) is solved numerically trough finite differences. At each dimensionless time step $t^{k+1} = t^k + \Delta t^k$, the migration of the ith node in the direction n normal to s is computed through a time marching procedure of the form (Crosato, 1990):

$$x_i^{k+1} = x_i^k - \Delta t_i^k \frac{\zeta_i^k + \zeta_i^{k-1}}{2} \sin\theta_i^k, \tag{12}$$

$$y_i^{k+1} = y_i^k + \Delta t_i^k \frac{\zeta_i^k + \zeta_i^{k-1}}{2} \cos\theta_i^k, \tag{13}$$

where $x_i^{k+1} = x_i(t^{k+1})$, $y_i^{k+1} = y_i(t^{k+1})$, and $\zeta_i^k = E_i^k\, U_{bi}^k$. The value θ_i^k of the local tangent angle is computed by backward and forward averaging (Lanzoni and Seminara, 2006):

$$\theta_i^k = \frac{1}{2}\Big(\arctan \frac{y_{i+1}^k - y_i^k}{x_{i+1}^k - x_i^k} + \arctan \frac{y_i^k - y_{i-1}^k}{x_i^k - x_{i-1}^k} \Big) \tag{14}$$

This angle is also used to discretize the geometrical relationship (3) and to determine

the local value of the dimensionless curvature $\mathcal{C}_i^k$:

$$\mathcal{C}_i^k = -\frac{1}{\nu_0}\,\frac{\theta_{i+1}^k - \theta_{i-1}^k}{2\Delta s_i^k} \tag{15}$$

where Δs_i^k is the dimensionless distance between two consecutive points. The possible numerical anomalies arising from the curvature computation (Schwenk et al., 2015) are filtered out by using a Savitzky-Golay smoothing filter (Orfanidis, 1995; Motta et al., 2012a). The time step size Δt_i^k is controlled by requiring that:

$$\Delta t_i^k \leq \alpha \left(\frac{\Delta s_i^k}{E_i^k U_{bi}^k} \right)_{\max} \tag{16}$$

where α is a parameter defining the threshold between stable and unstable computations, to be chosen empirically ($\alpha \sim 10^{-2}$) on the basis of a balance between computational effort and accuracy of the numerical solution (Crosato, 1990; Lanzoni and Seminara, 2006).

Since the deformation experienced by the channel axis at each time step leads to continuous variations of Δs_i^k, the mesh is periodically re-built to maintain quasi-uniformity of the node spacings, adding or removing nodes to maintain the value of Δs_i^k into the range 2/3 and 4/3.

The progressive elongation of the channel axis produces neck cutoffs, whereby the upstream and downstream portions of a bend loop approach each other and eventually intersect. The meander loop is then bypassed, and the older, more sinuous reach is abandoned by the active river, forming an oxbow lake when sedimentation closes its ends. These processes may last many years (Gagliano and Howard, 1984) but, because of the long time scales characterizing the evolution of the river planform, they can be assumed to occur instantaneously in the simulation model. Following Howard and Knutson (1984) and Sun et al. (1996), the presence of potential neck cutoffs is detected by controlling the dimensionless distance between a given point P_i and the nearby points P_{i+r} located sufficiently downstream (e.g., $r \geq 8$). This control is made through the algorithm developed by Camporeale et al. (2005) which improves the computational efficiency of the model. When the computed Cartesian distance between nodes P_i and P_{i+r} is lower than a threshold value, say $\Delta s_r = 2.2$, all the points P_{i+j}, $j = 1, r-1$ are removed from the computational grid, defining a

new oxbow lake (Figure 3). A few nodes upstream of P_i and downstream of P_{i+r} (e.g., P_{i-q}, P_{i+r+q}, $q = 1, 2, 3$) are also removed to prevent the formation of a high-curvature river reach (Frascati and Lanzoni, 2009) that, in nature, is unlikely to persist owing to the rapid smoothing action of the current and the along river propagation of the geometric disturbances generated by the cutoff even (Hooke, 1995; Camporeale et al., 2008).

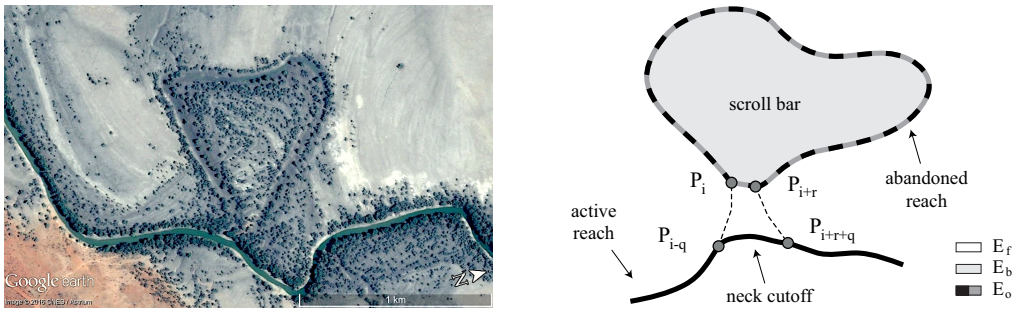

(a) Natural cutoff process. (b) Numerical cutoff process.

Figure 3: Example of (a) a natural neck cutoff process producing a different geomorphic environment inside the oxbow lake contour (Darling River, Australia, 31° 33' S 143° 30' E, source: Google Earth Pro), and of (b) the numerical modelling of neck cutoff occurrence, with the formation of two new environments, namely the oxbow lake formed by the abandoned reach and the inner scroll bar bounded by the previous element. Symbols are as follows: r determines the points that are considered to check the occurrence of a incipient neck cutoff; q is the number of point removed to avoid the presence of a high-curvature river reach after a cutoff; E_f, E_b, and E_o are the erodibility coefficients assigned to the pristine floodplain, the scroll bar environment and the oxbow lake environment, respectively.

The alternate form of cutoff, the chute cutoff, is not treated by this model.
As observed above, the total length of the channel and the bed slope change over time due to the elongation driven by migration and the shortening due to cutoff occurrences. As a consequence, suitable relations must be imposed in order to keep consistent steady flow and sediment transport conditions. Assuming a constant discharge and a temporally constant floodplain gradient, the relevant physical parameters between two

time steps k and $k+1$ are updated as follows:

$$\frac{\beta^{k+1}}{\beta^k} = \left(\frac{C_f^k}{C_f^{k+1}}\right)^{1/3}\left(\frac{\sigma_T^k}{\sigma_T^{k+1}}\right)^{1/3} \tag{17}$$

$$\frac{\tau_*^{k+1}}{\tau_*^k} = \left(\frac{C_f^k}{C_f^{k+1}}\right)^{-1/3}\left(\frac{\sigma_T^k}{\sigma_T^{k+1}}\right)^{2/3} \tag{18}$$

$$\frac{d_s^{k+1}}{d_s^k} = \left(\frac{C_f^k}{C_f^{k+1}}\right)^{1/3}\left(\frac{\sigma_T^k}{\sigma_T^{k+1}}\right)^{1/3} \tag{19}$$

where σ_T is the river sinuosity, defined as the ratio of the dimensionless intrinsic length $L = L^*/B_0^*$ (computed along the channel centerline) to the dimensionless Cartesian length $l_x = l_x^*/B_0^*$ (obtained projecting the river axis on the longitudinal axis x oriented in the direction of the floodplain gradient).

Floodplain features

The model described so far has been found to effectively reproduce typical meander shapes observed in nature (simple bends, compound bends and multiple loops) for a constant (in time and space) floodplain erodibility (Frascati and Lanzoni, 2009). The bank erosion coefficient, however, generally depends on soil properties, deposition and consolidation processes, groundwater dynamics (Han and Endreny, 2014), and distribution of riparian vegetation (Perucca et al., 2007; Motta et al., 2012a,b; Wickert et al., 2013). To mimic these heterogeneities, the valley surface is, as a first approximation, schematized by three different geomorphic units with different local coefficients E (Figure 3), depending on the soil properties as well as on the vegetation cover.

The first geomorphic unit is the pristine floodplain, with coefficient $E = E_f$. It corresponds to the undisturbed floodplain consisting of sediment deposited by repeated flooding events, not yet impacted and consequently reworked by the river migration.

The second geomorphic unit corresponds to the oxbow lake environment, with coefficient $E = E_o$. It mimics the fine-filled abandoned channel reach which leads to the formation of plugs that may obstruct the lateral migration of the active channel (Toonen et al., 2012). Finally, the third geomorphic unit corresponds to the scroll bar environment, with coefficient $E = E_b$. It mimics the floodplain area bounded by an oxbow lake, characterized by the typical ridge-and-swale sequence. In particular,

coarse-grained sediments typically accumulates on the ridge, while finer sediment (silt and clay) deposit in the upper part (Nanson, 1980) because of the temporary flow expansions (van De Lageweg et al., 2014). The structure of vegetation reflects the local topography and hydrological conditions (Zen et al., 2016) contributing to the erosional complexity of the scroll bodies.

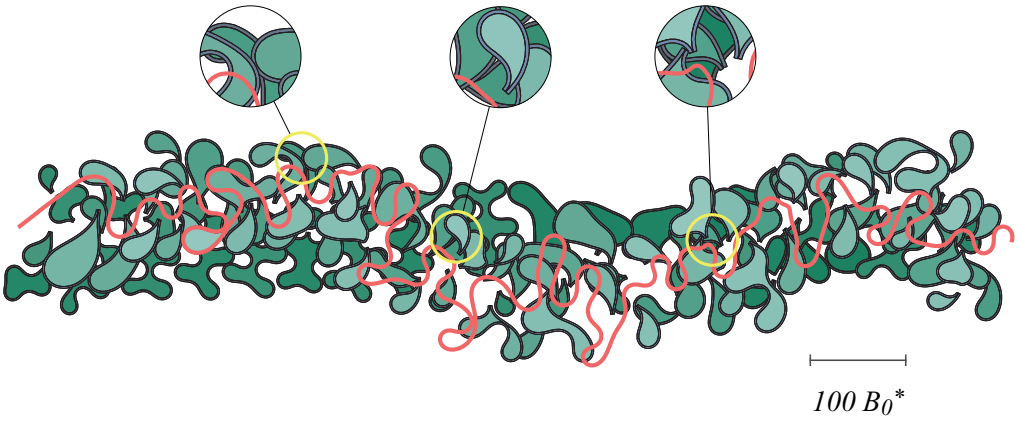

Figure 4: Example of a simulated planform dynamics, with the formation of scroll bars (older are dark green, younger are light green) and oxbow lakes (gray stripes bounding the previous elements, corresponding to the abandoned bends).

All the erosion coefficients are kept constant over time in order to maintain the modelling framework at the lowest possible level of complexity, thus temporal variations caused, e.g., by soil compaction and biological dynamics are not considered. Furthermore, incision, soil uplift, and subsidence are not accounted for, assuming that the floodplain surface is infinitely large and keeps its elevation constant over time. Possible changes in the hydrological regime and flow unsteadiness associated with flood waves are neglected as well.

Spatial variability ensuing from the meandering dynamics is accounted for as follows. All the progressively formed geomorphic environments (oxbow lakes and scroll bars) are saved as polygons given by the abandoned mesh nodes (Figure 4). As the generic node P_i of the active channel axis migrates laterally, the river may encounter three different environments during its lateral migration onto the valley. The winding number algorithm of Hormann and Agathos (2001) is used to identify whether the current

point lies within a pre-saved geomorphic unit and, hence, to choose the appropriate local erosion coefficient.

The flow field

This section briefly summarizes the key points of two mathematical models of channel morphodynamics implemented in the model, namely the model developed by Ikeda et al. (1981), hereafter referred to as IPS model, and the model developed by Zolezzi and Seminara (2001), hereafter referred to as ZS, similarly to the approach of Frascati (2009). Both models are based on the assumption of a secondary bidimensional flow driven by the curvature distribution and superimposed to the primary uniform flow travelling the channel.

The use of two models entailing a different level of approximation is motivated by the importance that the coupling of the flow field and the sediment balance equations has on the quantitative reproduction of observed river planforms. The former model however, assumes empirically the form of the channel cross-section.

The IPS model has been widely used (see, among the others, Perucca et al., 2005; Güneralp and Rhoads, 2011; Schuurman et al., 2016). The decoupling of the equations governing the flow field and the sediment conservation does not allow to solve for the bed configuration, thus an empirical relation is required. The dimensionless excess near-bank velocity U_b takes the type:

$$U_b = U_0^* \, F\left[\nu_0, \beta, C_f, \tau_*, \mathcal{C}, \int_0^s \mathcal{C}(\xi)\, e^{\lambda_0 (s-\xi)}\, d\xi\right] \tag{20}$$

where the characteristic exponent $\lambda_0 = -2\beta C_f$ drives the convolution integral which accounts for the effect of the upstream curvature distribution on the downstream reach (downstream influence).

The ZS morphodynamic model solves the steady flow field in a movable bed river with variable curvature of the channel axis. It was derived by integrating over the depth the continuity equation and the Reynolds-averaged Navier-Stokes equations (RANS), written in intrinsic coordinates, and by introducing a parametrization of the secondary flow driven by the channel axis curvature (Zolezzi and Seminara, 2001). The extension of the model to cases involving width variations was developed by Frascati and Lan-

zoni (2013). The resulting equations are fully coupled to the Exner sediment balance equation, also written in curvilinear coordinates, and closed by means of a suitable sediment transport law. All the relevant equations are then linearized, by expanding in terms of small parameters, taking advantage of the typically wide character of river bends (small curvature ratio ν_0). Eventually, the following functional relationship is found:

$$U_b = U_0^* F\left[\nu_0, \beta, C_f, \tau_*, \mathcal{C}, \int_0^s \mathcal{C}(\xi)\, e^{\lambda_{mj}(s-\xi)}\, d\xi\right] \tag{21}$$

where λ_{mj} $(m = 0, \infty; j = 1, 4)$ are characteristic exponents for the mth lateral Fourier mode which are crucial to determine, through the related convolution integrals, whether flow and bed topography at a given position s are affected by the river reach located upstream (downstream influence) or downstream (upstream influence) (Zolezzi and Seminara, 2001; Lanzoni and Seminara, 2006). The four exponents are the solutions of the four-order ordinary differential equation that arises from the linearized continuity and momentum equations coupled with the sediment balance equation. Figure 5 shows three examples of the trends followed by the characteristic exponents λ_{mj} as functions of the values of the half width to depth ratio β, compared with the behaviour of the characteristic exponent λ_0 resulting from the IPS approach. It is worthwhile to note that, generally, λ_{m1} is real positive, λ_{m4} is real negative. They describe non-oscillatory spatial perturbations which decay fairly fast either downstream or upstream. The other two exponents λ_{m2} and λ_{m3} are complex conjugate, having respectively equal real parts ($\lambda_{m2r} = \lambda_{m3r}$) and opposite imaginary parts $\lambda_{m2i} = -\lambda_{m3i}$. They describe oscillatory spatial perturbations which decay fairly slowly, spreading their influence over a considerable channel length (Lanzoni et al., 2006). Moreover, λ_{m3r} can be negative or positive, depending whether the aspect ratio β is smaller or larger than a threshold value, β_r . Channels characterized by aspect ratios $\beta < \beta_r$ are defined subresonant, leading to a downstream influence, as in the IPS model. On the contrary, channels characterized by aspect ratios $\beta > \beta_r$ are defined superresonant, leading to a upstream influence. This latter condition can not emerge when using the IPS model, as the latter is driven by a first-order ordinary differential equation because of the uncoupling of the sediment balance equation and the flow field. Subresonant

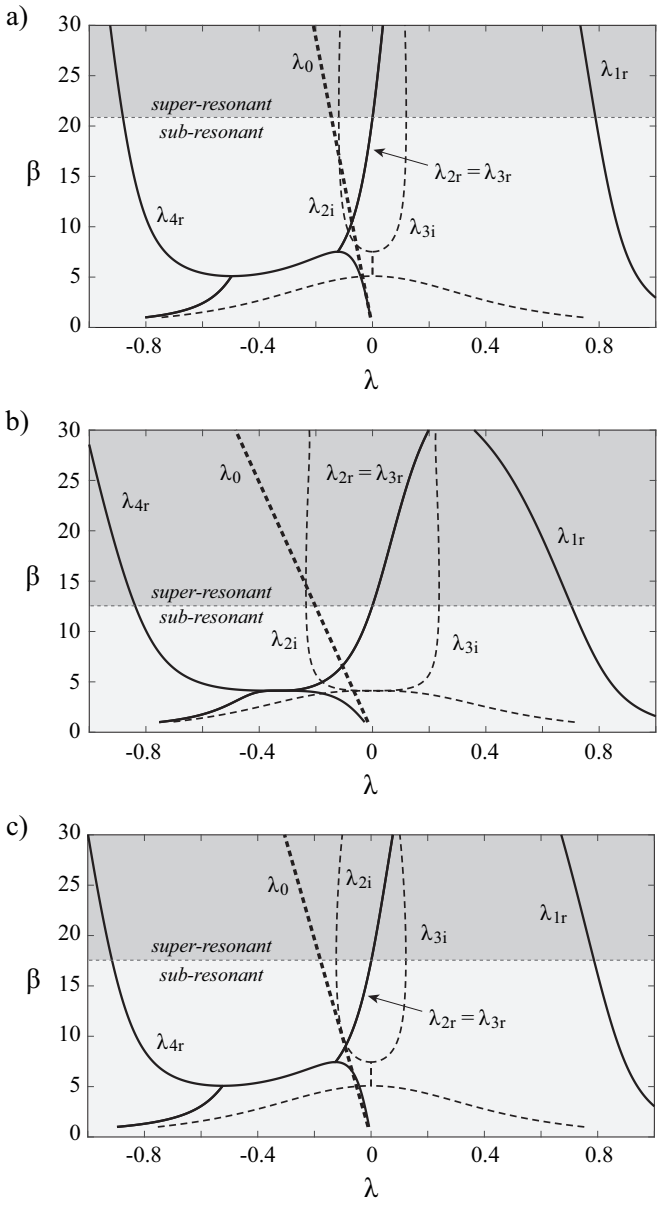

Figure 5: Typical behaviour of the four characteristic exponents λ_{mj} of the ZS approach as a function of the half width to depth ratio β, for three different scenarios. Continuous lines correspond to the real parts, dashed thin lines correspond to the imaginary parts, while the dashed thick line corresponds to the characteristic exponent λ_0 of the IPS approach. The three scenarios are characterized by the following parameter sets: a) $\tau_* = 0.1$, $d_s = 0.005$, flat bed; b) $\tau_* = 0.3$, $d_s = 0.001$, dune-covered bed; c) $\tau_* = 0.6$, $d_s = 0.0001$, dune-covered bed.

meanders are typically upstream skewed and migrate downstream, while superresonant meanders are typically downstream skewed and migrate upstream (Lanzoni et al., 2006; Lanzoni and Seminara, 2006).

Further details about the derivation, performances, and limitations inherent in linearization of the flow field model may be found in Zolezzi and Seminara (2001) and Frascati and Lanzoni (2013).

In order to increase the computational efficiency in the numerical implementation, the convolution integrals appearing in the expressions for the velocity perturbation (20) and (21) are evaluated using Simpson rule, truncating the integration when the function to be integrated, that decayes exponentially, is smaller than a given tolerance, say 10^{-4} (Lanzoni and Seminara, 2006).

Part I

Input files

3 File SIM

The SIM file is a formatted text file containing the leading parameters of the flow filed computation, the structure of the floodplain and the simulation parameters.
Variable types are as follows:

- I : integer variable,
- R : double precision variable (real∗8)
- S : integer switch
- T_n : text with n maximum types.

Row	**Variable**	**Type**	**Description**
1			*Text row*
2	<SIM name>	T_{20}	simulation name (max 20 letters)
3			*Text row*
4	β	R	half width to depth ratio
5	τ^*	R	Shields number
6	d_s	R	dimensioless grain roughness
7	flagbed	S	source for bed configuration 1:from R_p; 2:from typebed
8	R_p	R	Reynolds particle number
9	typebed	S	fixed bed configuration 1:flat bed; 2:dune-covered
10	r	R	transverse transport parameter (Talmon 1995)
11	jmodel	S	flow field model 1: ZS approach; 2: IPS approach
12	N_z	I	number of points for the vertical flow integration in ZS model
13	M_{dat}	I	order of the Fourier expansion in ZS model

File SIM continues on next page

File SIM continues from previous page

Row	Variable	Type	Description
14			*Text row*
15	E_f	R	erodibility coefficient of the floodplain
16	E_b	R	erodibility coefficient of the point bars
17	E_o	R	erodibility coefficient of the oxbow lakes
18	flag_{ox}	S	flag for existing structure of the floodplain 0: no; 1: yes
19			*Text row*
20	N_0	I	initial number of points
21	flag_{xy0}	S	initial planform configuration 1: straight path randomly perturbed; 2: given configuration from filexy
22	filexy	T_{20}	name of geometry file with dimensionless coordinates (maximum 20 letters)
23	Δs	R	resampling distance between axis points
24	$\Delta s_{\min}$	R	minimum allowed value of grid size (times Δs)
25	$\Delta s_{\max}$	R	maximum allowed value of grid size (times Δs)
26	N_{rand}	I	number of point interested by a slight perturbation if $\text{flag}_{\text{xy0}} = 1$
27	*stdv*	R	standard deviation of initial perturbation if $\text{flag}_{\text{xy0}} = 1$
28	toll_c	R	minimum threshold before neck-cutoff
29	j_{re}	I	points removed upstream and downstream of a cutoff
30	j_{nco}	I	minimum threshold points for neck cutoff searching (> 2)
31	k_{savgol}	I	SavitzkyGolay flag

File SIM continues on next page

File SIM continues from previous page

Row	Variable	Type	Description
			< 0: number of smoothing repetitions in each iteration (absolute value); > 0: iteration wait between two smoothings; 0: no smoothing.
32			*Text row*
33	$\text{flag}_{\text{time}}$	S	flag for defining the end of the simulation 1: time; 2: coefficient multiplying the time of first cutoff; 3: number of iterations; 4: number of cutoffs; 5: number of printed configurations.
34	TT_s	R	simulation time if $\text{flag}_{\text{time}} = 1$ (dimensionless years)
35	$k_{TT_{fco}}$	R	coefficient for first cutoff time if $\text{flag}_{\text{time}} = 2$
36	n_{end}	I	item number if $\text{flag}_{\text{time}} \geq 3$ (number of iterations / number of cutoffs / number of printed configurations)
37	tt_0	R	starting time (dimensionless years)
38	$flag_{dt}$	S	flag for time marching 1: fixed and equal to dt_0; 2: dynamic but always $< dt_0$.
39	dt_0	R	fixed time step (dimensionless years)
40	c_{stab}	R	coefficient for time marching
41	i_{video}	I	iterations between two screen prints
42	i_{screen}	I	iterations between two file prints

End of file SIM

4 File XY

File `XY` contains the initial geometrical path of the computational domain, scaled with the half width B_0^*. This text file consists of a matrix with N_0 rows, i.e. one row per node, and 2 columns which are the dimensionless longitudinal coordinate $x = x^*/B_0^*$ and the transverse coordinate $y = y^*/B_0^*$, respectively.

x_1	y_1
x_2	y_2
$\dots$	$\dots$
x_{N_0}	y_{N_0}

Part II

Output files

5 File SIMULATION

File <SIM NAME> _SIMULATION.DAT records the temporal trends of some geometrical parameters, i.e. number of points forming the river axis, number of floodplain features. This file consists of a matrix with nt rows, i.e. one row per printed time step, and 7 columns which are specified in the table below.

Column index	**Variable**	**Description**
1	j_p	index of the current printed step
2	j_t	iteration index
3	t	dimensionless time of the current step
4	N	number of points forming the channel axis
5	N_{pb}	current total number of axis points within the scroll bar environments
6	N_{po}	current total number of axis points within the oxbow lake environments
7	N_{nco}	cumulate number of neck cutoffs

6 File PARAMETERS

File <SIM NAME> _PARAMETERS.DAT records the temporal trends of the leading morphodynamic parameters. This file consists of a matrix with nt rows, i.e. one row per printed time step, and 10 columns which are specified in the table below.

Column index	**Variable**	**Description**
1	j_p	index of the current printed step
2	j_t	iteration index
3	t	dimensionless time of the current step
4	$L = L^*/B_0^*$	dimensionless length of the current channel path, scaled by the half width
5	β	half width to depth ratio
6	$\tau*$	Shields number
7	d_s	grain size to depth ratio
8	C_f	friction coefficient
9	typebed	bed configuration (1: flat bed, 2: dune-covered)
10	typeload	sediment flux type (1: bedload 2: total load)

7 File CUTOFFS

File <SIM NAME> _CUTOFFS.DAT records the temporal trends of the cutoff occurrences. This file consists of a matrix with n_{nco} rows, i.e. one row per cutoff occurrence, and 10 columns which are specified in the table below.

Column index	**Variable**	**Description**
1	j	index of the current neck cutoff occurrence
2	N_{rem}	number of point forming the abandoned bend
3	N	former number of axis points
4	j_{up}^{ch}	last node of the channel axis upstream of the cutoff
5	j_{up}^{co}	upstream node of the cutoff
6	j_{dw}^{co}	downstream node of the cutoff
7	j_{dw}^{ch}	first node of the channel axis downstream of the cutoff
8	N_{new}	new number of axis points
9	t	dimensionless time of the current step
10	j_t	iteration index

8 File CONFIGURATION

File `CONFIGURATION_ <jt>.OUT` contains the geometrical features of the computational domain at the printing step jp which corresponds to the instant time t, basing on file `SIMULATION`. This file consists of a matrix with nn rows, i.e. one row per node, and 6 columns which are specified in the table below.

Column index	**Variable**	**Description**
1	$x = x^*/B_0^*$	dimensionless longitudinal coordinate
2	$y = y^*/B_0^*$	dimensionless transverse coordinate
3	$s = s^*/B_0^*$	dimensionless intrinsic coordinate
4	$-\theta$	negative local angle of the axis river with the longitudinal direction
5	$\nu_0\mathcal{C}$	dimensionless local curvature
6	$U_b = \dfrac{U^*\big\vert_{n=1} - U^*\big\vert_{n=-1}}{U_0^*}$	dimensionless excess near-bank velocity

9 File OXBOW

File `OXBOW_<j>.OUT` contains the geometrical path of the current oxbow lake, scaled with the half width B_0^*. This text file consists of a matrix with N_{ox} rows, i.e. one row per node, and 2 columns which are the dimensionless longitudinal coordinate $x = x^*/B_0^*$ and the transverse coordinate $y = y^*/B_0^*$ forming the oxbow lake, respectively.

x_1	y_1
x_2	y_2
$\dots$	$\dots$
$x_{N_{ox}}$	$y_{N_{ox}}$

10 File POINTBAR

File `POINT_BAR_<j>.OUT` contains the geometrical path of the current point bar, scaled with the half width B_0^*. This text file consists of a matrix with N_{pb} rows, i.e. one row per node, and 2 columns which are the dimensionless longitudinal coordinate $x = x^*/B_0^*$ and the transverse coordinate $y = y^*/B_0^*$ forming the point bar, respectively.

x_1	y_1
x_2	y_2
$\dots$	$\dots$
$x_{N_{pb}}$	$y_{N_{pb}}$

11 File LAMBDA

File <SIM NAME>_LAMBDA.DAT records the temporal trends of the characteristic eigenvalues of the mathematical model for the curvature-driven flow field.
When the flow field is computed by the IPS model, this file consists of a matrix with nt rows, i.e. one row per printed time step, and 4 columns which are specified in the table below.

Column index	**Variable**	**Description**
1	j_p	index of the current printed step
2	j_t	iteration index
3	t	dimensionless time of the current step
4	λ_0	characteristic exponent of the IPS model

When the flow field is computed by the ZS model, this file consists of a matrix with $nt \times M_{dat}$ rows, i.e. M_{dat} rows per printed time step where M_{dat} is the order of the Fourier expansion in ZS model, and 12 columns which are specified in the table below.

Column index	**Variable**	**Description**
1	j_p	index of the current printed step
2	j_t	iteration index
3	j_m	current Fourier mode
4	t	dimensionless time of the current step
5	$Re(\lambda_{m1})$	real part of the first characteristic exponent of the ZS model
6	$Im(\lambda_{m1})$	imaginary part of the first characteristic exponent of the ZS model
7	$Re(\lambda_{m2})$	real part of the second characteristic exponent of the ZS model
8	$Im(\lambda_{m2})$	imaginary part of the second characteristic exponent of the ZS model
9	$Re(\lambda_{m3})$	real part of the third characteristic exponent of the ZS model
10	$Im(\lambda_{m3})$	imaginary part of the third characteristic exponent of the ZS model
11	$Re(\lambda_{m4})$	real part of the fourth characteristic exponent of the ZS model
12	$Im(\lambda_{m4})$	imaginary part of the fourth characteristic exponent of the ZS model

Part III

Other files

12 File XY TEMP

File `XY.DAT` is a text file containing the backup data of the last iteration. The header lines contain the last update of the leading parameters:

- j_t : last iteration index;
- t : dimensionless time of the current step;
- β : half width to depth ratio;
- $\tau*$: Shields number;
- d_s : grain size to depth ratio;
- C_f : friction coefficient;
- j_p : index of the current printed step;
- N : number of points forming the channel axis;
- text line.

The file contains also a matrix with N rows, i.e. one row per node, and 2 columns which are the dimensionless longitudinal coordinate $x = x^*/B_0^*$ and the transverse coordinate $y = y^*/B_0^*$, respectively.

x_1	y_1
x_2	y_2
...	...
x_N	y_N

13 Files FLOODPLAIN

The following files are generated and updated by the numerical code during the simulation runs, and they are required for a future new simulation which involves an existing floodplain structure.

- File <SIM NAME> _NNCO.dat contains the number of cutoffs occurred so far.
- Files <SIM NAME> _PB.dat contain the storage indices defining the point bar arrays.
- Files <SIM NAME> _OX.dat contain the storage indices defining the oxbow lake arrays.

14 File TIME

File <SIM NAME> _TIMESIM.DAT recors the date and time of beginning and end of the simulation, as well as the simulation duration.

References

Asahi, K., Shimizu, Y., Nelson, J., and Parker, G. (2013). Numerical simulation of river meandering with self-evolving banks. *Journal of Geophysical Research: Earth Surface*, 118:2208–2229.

Bogoni, M. (2017). *Long-term evolution of meandering rivers flowing above heterogeneous floodplains*. PhD thesis.

Camporeale, C., Perona, P., Porporato, A., and Ridolfi, L. (2005). On the long-term behavior of meandering rivers. *Water Resources Research*, 41(12):1–13.

Camporeale, C., Perucca, E., and Ridolfi, L. (2008). Significance of cutoff in meandering river dynamics. *Journal of Geophysical Research: Earth Surface*, 113(1):1–11.

Crosato, A. (1990). Simulation of meandering river process. Technical Report 3, Delft university of Tecnology, Delft (NL), Delft.

Eke, E. C., Parker, G., and Shimizu, Y. (2014). Numerical modeling of erosional and depositional bank processes in migrating river bends with self-formed width: morphodynamics of barp ush and bank pull. *Journal of Geophysical Research: Earth Surface*, 119(2):1–29.

Engelund, F. and Hansen, E. (1967). A monograph on sediment transport in alluvial stream. Technical report, Technical University of Denmark, Copenhagen.

Frascati, A. (2009). *Morphodynamic regime and long-term modelling of meandering rivers*. PhD thesis.

Frascati, A. and Lanzoni, S. (2009). Morphodynamic regime and long-term evolution of meandering rivers. *Journal of Geophysical Research: Earth Surface*, 114(2):1–12.

Frascati, A. and Lanzoni, S. (2010). Long-term river meandering as a part of chaotic dynamics? A contribution from mathematical modelling. *Earth Surface Processes and Landforms*, 35(7):791–802.

Frascati, A. and Lanzoni, S. (2013). A mathematical model for meandering rivers with varying width. *Journal of Geophysical Research: Earth Surface*, 118(3):1641–1657.

Gagliano, S. M. and Howard, P. C. (1984). The neck cutoff oxbow lake cycle along the Lower Mississippi River. In CM, E., editor, *River Meandering, Proceedings of the Conference Rivers 1983*, pages 147–158. ASCE. New Orleans.

Güneralp, Í. and Rhoads, B. L. (2011). Influence of floodplain erosional heterogeneity on planform complexity of meandering rivers. *Geophysical Research Letters*, 38(14):2–7.

Han, B. and Endreny, T. (2014). Detailed river stage mapping and head gradient analysis during meander cutoff in a laboratory river. *Water Resources Research*, 50:1689–1703.

Hooke, J. M. (1995). River channel adjustment to meander cutoffs on the River Bollin and River Dane, northwest England. *Geomorphology*, 14(3):235–253.

Hormann, K. and Agathos, A. (2001). The point in polygon problem for arbitrary polygons. *Computational Geometry: Theory and Applications*, 20(3):131–144.

Howard, A. D. and Knutson, T. R. (1984). Sufficient conditions for river meanering: a simulation approach. *Water Resources Research*, 20(11):1659–1667.

Ikeda, S., Parker, G., and Sawai, K. (1981). Bend theory of river meanders. Part 1. Linear development. *Journal of Fluid Mechanics*, 112:363–377.

Lanzoni, S. and Seminara, G. (2006). On the nature of meander instability. *Journal of Geophysical Research*, 111(4):1–14.

Lanzoni, S., Siviglia, A., Frascati, A., and Seminara, G. (2006). Long waves in erodible channels and morphodynamic influence. *Water Resources Research*, 42:1–15.

Motta, D., Abad, J. D., Langendoen, E. J., and Garcia, M. H. (2012a). A simplified 2d model for meander migration with physically-based bank evolution. *Geomorphology*, 163:10–25.

Motta, D., Abad, J. D., Langendoen, E. J., and García, M. H. (2012b). The effects of floodplain soil heterogeneity on meander planform shape. *Water Resources Research*, 48(9):1–17.

Nanson, G. C. (1980). Point bar and floodplain formation of the meandering Beatton River, northeastern British Columbia, Canada. *Sedimentology*, 27(1):3–29.

Orfanidis, S. J. (1995). *Introduction to signal processing*. Prentice-Hall, Inc.

Parker, G. (1990). Surface-based bedload transport relation for gravel rivers. *Journal of Hydraulic Research*, 28(4):417–436.

Parker, G., Shimizu, Y., Wilkerson, G. V., Eke, E. C., Abad, J. D., Lauer, J. W., Paola, C., Dietrich, W. E., and Voller, V. R. (2011). A new framework for modeling the migration of meandering rivers. *Earth Surface Processes and Landforms*, 36(1):70–86.

Perucca, E., Camporeale, C., and Ridolfi, L. (2005). Nonlinear analysis of the geometry of meandering rivers. *Geophysical Research Letters*, 32(3):1–4.

Perucca, E., Camporeale, C., and Ridolfi, L. (2007). Significance of the riparian vegetation dynamics on meandering river morphodynamics. *Water Resources Research*, 43(3):1–10.

Schuurman, F., Shimizu, Y., Iwasaki, T., and Kleinhans, M. G. (2016). Dynamic meandering in response to upstream perturbations and floodplain formation. *Geomorphology*, 253:94–109.

Schwenk, J., Lanzoni, S., and Foufoula-Georgiou, E. (2015). The life of a meander bend : connecting shape and dynamics via analysis of a numerical model. *Journal of Geophysical Research: Earth Surface*, 120:690–710.

Seminara, G., Zolezzi, G., Tubino, M., and Zardi, D. (2001). Downstream and upstream influence in river meandering. Part 2. Planimetric development. *Journal of Fluid Mechanics*, 438:213–230.

Sun, T., Meakin, P., Jøssang, T., and Schwarz, K. (1996). A simulation model for meandering rivers. *Water Resources Research*, 32(9):2937–2954.

Toonen, W. H., Kleinhans, M. G., and Cohen, K. M. (2012). Sedimentary architecture of abandoned channel fills. *Earth Surface Processes and Landforms*, 37(4):459–472.

van De Lageweg, W. I., van Dijk, W. M., Baar, A. W., Rutten, J., and Kleinhans, M. G. (2014). Bank pull or bar push : What drives scroll-bar formation in meandering rivers ? *Geology*, pages 1–4.

Van Rijn, L. C. (1984a). Sediment transport, part II: suspended load transport. *Journal of Hydraulic Engineering*, 110(11):1613–1641.

Van Rijn, L. C. (1984b). Sediment transport, part III: bed forms and alluvial roughness. *Journal of Hydraulic Engineering*, 110(12):1733–1754.

Wickert, A. D., Martin, J. M., Tal, M., Kim, W., Sheets, B., and Paola, C. (2013). River channel lateral mobility: Metrics, time scales, and controls. *Journal of Geophysical Research: Earth Surface*, 118(2):396–412.

Zen, S., Zolezzi, G., Toffolon, M., and Gurnell, A. M. (2016). Biomorphodynamic modelling of inner bank advance in migrating meander bends. *Advances in Water Resources*, 93:166–181.

Zolezzi, G. and Seminara, G. (2001). Downstream and upstream influence in river meandering. Part 1. General theory and application to overdeepening. *Journal of Fluid Mechanics*, 438:183–211.